Combined experimental and theoretical study of fast atom diffraction on the $\beta_2(2\times4)$ reconstructed GaAs(001) surface

M. Debiossac, A. Zugarramurdi, H. Khemliche, P. Roncin,* and A. G. Borisov
Institut des Sciences Moléculaires d'Orsay, UMR 8214 CNRS–Université Paris-Sud, Bât. 351, Université Paris-Sud, 91405 Orsay CEDEX, France

A. Momeni
Institut des Sciences Moléculaires d'Orsay, UMR 8214 CNRS–Université Paris-Sud, Bât. 351, Université Paris-Sud, 91405 Orsay CEDEX, France and Université de Cergy-Pontoise, 33 Boulevard du Port, F-95031 Cergy, France

P. Atkinson,* M. Eddrief, and F. Finocchi
Sorbonne Universités, UPMC Univ Paris 06, UMR 7588, Institut des Nanosciences de Paris, F-75005, Paris, France and CNRS, UMR 7588, Institut des Nanosciences de Paris, F-75005, Paris, France

V. H. Etgens
VeDeCom - Université Versailles Saint-Quentin en Yvelines, 77 rue des Chantiers, 78000 Versailles, France
(Received 25 July 2014; revised manuscript received 12 September 2014; published 15 October 2014)

A grazing incidence fast atom diffraction (GIFAD or FAD) setup, installed on a molecular beam epitaxy chamber, has been used to characterize the $\beta_2(2\times4)$ reconstruction of a GaAs(001) surface at 530 °C under an As_4 overpressure. Using a 400-eV ^{4}He beam, high-resolution diffraction patterns with up to eighty well-resolved diffraction orders are observed simultaneously, providing a detailed fingerprint of the surface structure. Experimental diffraction data are in good agreement with results from quantum scattering calculations based on an *ab initio* projectile-surface interaction potential. Along with exact calculations, we show that a straightforward semiclassical analysis allows the features of the diffraction chart to be linked to the main characteristics of the surface reconstruction topography. Our results demonstrate that GIFAD is a technique suitable for measuring in situ the subtle details of complex surface reconstructions. We have performed measurements at very small incidence angles, where the kinetic energy of the projectile motion perpendicular to the surface can be reduced to less than 1 meV. This allowed the depth of the attractive van der Waals potential well to be estimated as −8.7 meV in very good agreement with results reported in literature.

DOI: 10.1103/PhysRevB.90.155308 PACS number(s): 34.35.+a, 68.49.Bc, 34.50.Cx

I. INTRODUCTION

The reconstruction of a surface largely determines its interaction with the environment affecting the growth of subsequent overlayers. Since thin films and sharp interfaces remain a technological challenge, significant research has been devoted to accurately measure and predict the detailed surface structure, in particular at elevated temperatures where thin film growth is usually conducted. Experimentally, electron diffraction techniques, such as low-energy electron diffraction (LEED) [1] and reflection high-energy electron diffraction (RHEED) [2–4], provide a simple and practical means to access basic crystallographic properties (symmetry, lattice parameter). In addition, RHEED is compatible with the real time analysis of conventional thin-film growth techniques such as molecular beam epitaxy (MBE). However, due to the importance of electron multiple scattering, a comparatively complex dynamical scattering theory is required to determine the atomic positions from RHEED data. In contrast, x-ray diffraction is well described by kinematical theory, which assumes that each photon is scattered only once, and is considered as the reference technique for the accurate determination of complex structural information [5,6]. The only limitation is that, due to the large x-ray mean free path, surface sensitivity is achieved only at grazing incidence (GIXRD), which requires high fluxes available only at synchrotron radiation facilities.

A less commonly used alternative is thermal energy helium atom scattering [7–10] (HAS) where the probing atoms are repelled by the surface, a few angstroms above the terminal layer, thus ensuring exclusive surface sensitivity of the diffraction pattern. HAS has been used to benchmark theoretical descriptions of gas-surface interactions [11–13] as well as the surface arrangement of atoms. However, the diffracted intensity, governed by the Debye-Waller factor, tends to vanish as soon as the helium wavelength becomes comparable to the amplitude of the thermal fluctuation of the surface atoms. For this reason, most HAS studies have been performed on nitrogen cooled surfaces and with helium atom energies below 60 meV [12,14]. Thus surface reconstructions, which occur at elevated temperatures, cannot be analyzed. Moreover, as a consequence of the low collision energy, the HAS is affected by the polarization van der Waals (vdW) interaction between the probe atom and the surface, which somewhat complicates the interpretation of the data [11,12,15–18].

More recently, a new diffraction regime has been identified [19–22] using fast helium atoms in the keV range, and a grazing incidence geometry similar to that of RHEED. Since the scattering of the fast helium atoms occurs over

*Corresponding authors: Philippe.roncin@u-psud.fr; atkinson@insp.jussieu.fr

tens of successive surface atoms, the thermal decoherence is drastically reduced [23–26] and, unlike HAS, diffraction can be observed at elevated temperatures and/or higher effective energies. Well-resolved diffraction patterns have been reported for dielectric [20–22], semiconductor [27,28], and metal surfaces [29,30]. Since these first observations, GIFAD has been used to obtain valuable information on the surface structure and reconstruction [22,30–37]. In practice, just as in RHEED, the whole diffraction cone is recorded at once on an imaging detector allowing real-time monitoring of semiconductor growth, as we recently demonstrated for GaAs [28].

In the present work, we show the ability of GIFAD to provide high-resolution diffraction images for the case of a large surface cell and strong surface corrugation giving rise to numerous diffracted beams. For this purpose we have selected the well-documented $\beta_2(2\times4)$ reconstruction of the GaAs(001) surface [2–4,14] stable around 500–580 °C under an arsenic overpressure $>10^{-6}$ mbar, which is known to have corrugation exceeding 3 Å. Experimental results are compared with quantum scattering calculations. As an input for the theoretical study of diffraction we use the interaction potential between a He projectile and the reconstructed GaAs(001) surface computed through the density functional theory (DFT). The paper is organized as follows. Section II describes the experiment and details the theoretical calculations. Section III is devoted to the results and their discussion, and finally, Sec. IV presents summary and conclusions. Atomic units (a.u.) are used throughout the paper unless otherwise stated.

II. METHODS

A. Experiment

The GIFAD neutral helium source is made of a commercial hot filament ion gun where He^+ ions are produced and extracted at the desired voltage, here 400 eV. These ions pass through a neutralization cell where approximately 10% become neutral as a result of resonant charge exchange with the helium background gas before exiting via a tiny diaphragm of diameter D_1. This diaphragm serves two purposes, it limits gas flooding from the cell towards the beam line and it defines the source extension of the neutral helium beam. At a distance $L_1 = 50$ cm downstream from D_1, another variable aperture, of a diameter D_2 limits the angular divergence to $\Delta\phi = (D_1 + D_2)/2L_1$. For typical values of 50 μm for both D_1 and D_2, the angular divergence is 10^{-4} rad (5.7 mdeg). This final aperture D_2 is located inside the growth chamber at a distance $L_2 = 10$ cm from the center of the GaAs wafer mounted on a rotatable sample holder. The ions that have not been neutralized are deflected away by a weak steering electric field at the exit of the neutralization cell (Fig. 1). The whole beam line is attached to the MBE chamber via a gate valve and a flexible bellows, with stepper motors controlling both the beam position and the angle of incidence. After grazing reflection on the GaAs wafer, the diffracted helium beam is collected at $L_3 = 95$ cm downstream on an imaging detector made of a pair of microchannel plates which convert the impact of helium atoms into an electron cascade accelerated onto a conventional phosphor screen mounted on a UHV glass viewport (Photonis

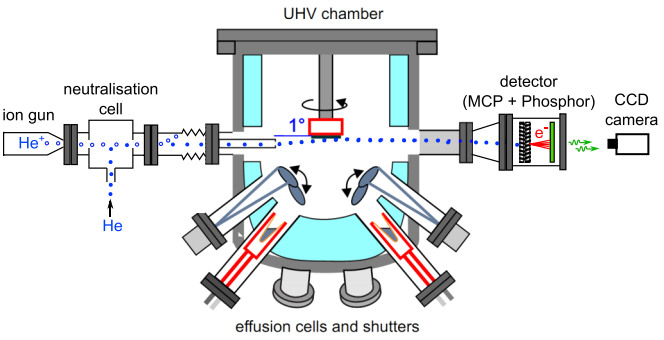

FIG. 1. (Color online) Schematic representation of the experimental setup showing a GIFAD ion source, consisting of an ion gun and neutralization chamber mounted by a flexible bellows onto an MBE growth chamber, shown here in side view. The angle of incidence of the atom beam on the sample is $\phi_{in} < 1°$. The imaging detector is mounted on the opposite side of the chamber, and consists of two microchannel plates, a phosphor screen and a CDD camera.

APD 3075FM). Outside the vacuum chamber, a low noise CCD camera (Hamamatsu C8484-05) records up to ten diffraction images per second [28] without dead time due to interline features. This system allows single-particle detection if the atomic flux is low enough while also allowing atomic fluxes as high as 10^6 atoms per second to be recorded without saturation of the CCD detector. The spatial calibration of the optical system was measured to be 67μm per CCD pixel, which corresponds to an angular calibration of 0.004° per pixel.

The GaAs surfaces used here are undoped GaAs(001) substrates (miscut <0.1°). Following thermal deoxidation at 600 °C, a thick (>200 nm) GaAs buffer layer was grown at 550 °C, and then annealed under As_4 at this temperature for one hour. GIFAD measurements were then carried out with the GaAs surface held at 530 °C, under an As_4 beam-equivalent-pressure of 10^{-6} mbar, corresponding to an arrival rate of 2×10^{14} As_4 molecules $cm^{-2}s^{-1}$ as calibrated by Arsenic RHEED oscillations. *Ex situ* atomic force measurements carried out after growth showed that the surface consisted of large GaAs terraces, typically larger than 500 nm in the [110] direction and larger than 1 μm in the [1$\bar{1}$0] direction. Under our experimental conditions, the GaAs(001) surface is in the $\beta_2(2\times4)$ reconstruction [2–4] as further confirmed by the analysis of GIFAD data presented below. Figure 2 gives a schematic representation of the reconstructed surface, and indicates the main crystallographic directions. The unit cell is large ($L_x \times L_y = 15.98$ Å$\times 7.99$ Å) and it can be seen that there is a pronounced axial channel along the [1$\bar{1}$0] direction with a corrugation exceeding one GaAs monolayer.

The scattering geometry is sketched in Fig. 3. The helium atom beam of energy E and momentum $k = \sqrt{2ME}$ (M stands for the projectile mass) impinges the $\beta_2(2\times4)$ reconstructed GaAs(001) surface at a grazing polar incidence angle ϕ and at (small) azimuthal misalignment angle Γ measured from the low-index direction. The z axis is pointing into the vacuum, and it is perpendicular to the surface (x, y) plane. In the experiments presented here, the beam was aligned close to the [1$\bar{1}$0] axial channel oriented along the y axis in Fig. 3. We have also observed well resolved diffraction patterns for the incidence

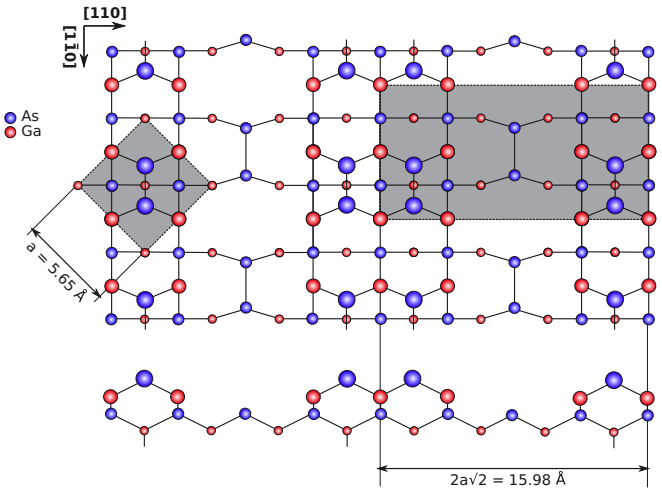

FIG. 2. (Color online) Schematic representation of the $\beta_2(2\times4)$ reconstruction of the GaAs(001) surface. The atomic arrangement plotted in the bottom is the one probed when the beam is aligned along the [1$\bar{1}$0] direction. The left gray square shows the projected bulk unit cell while the gray rectangle shows the reconstructed surface unit cell. Topmost atoms are represented with larger radii.

along the [110] axial channel. However, the effective surface corrugation as seen by the projectiles is quite low in this case resulting in a small number of populated diffraction orders and mild variations of the diffracted intensities with incident conditions. In the following, we concentrate exclusively on

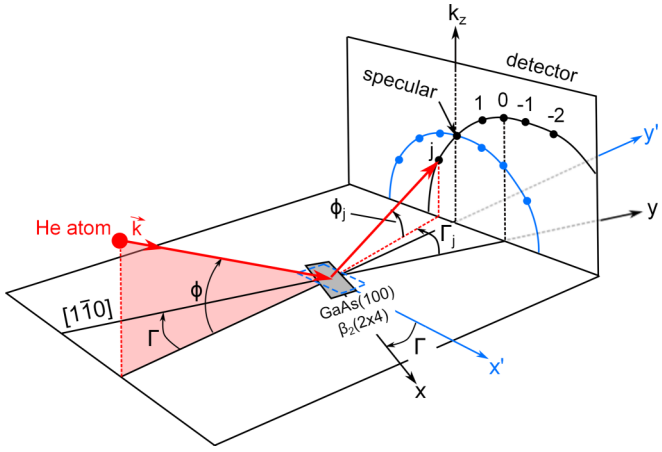

FIG. 3. (Color online) Sketch of the scattering geometry. A helium atom of momentum k impinges the $\beta_2(2\times4)$ reconstructed GaAs(001) surface. ϕ stands for the polar incidence angle and Γ stands for the azimuthal incidence angle. The Γ angle is measured with respect to the low-index [1$\bar{1}$0] direction. The diffracted beams leave the surface at exit angles ϕ_j and Γ_j detected in the momentum space (k_x,k_z). The index j stands for the diffraction order. Note that to be consistent with the convention used in the quantum scattering formalism, $j=0$ is taken to be the diffraction spot in the axial channeling direction, rather than the specular spot. The blue Laue circle corresponds to the case where the low-index direction at the surface is perfectly aligned the incident beam, whereas the black one corresponds to a misalignment angle Γ of two lattice vectors G through the relation $\sin(\Gamma) = 2G/k$.

the diffraction observed with the atom beam incident along the [1$\bar{1}$0] direction. Here, the greater surface corrugation gives rise to a more complex diffraction pattern allowing a more sensitive comparison between experimental data and theoretical calculations.

The motion of the projectiles perpendicular to the surface (z axis) is slow, and is characterised by energy $E_\perp = E\sin^2\phi$, and momentum component $k_z = k\sin(\phi) = \sqrt{2ME_\perp}$. The motion parallel to the surface is fast with momentum $k_\parallel \sim k$. In this paper, we use the axial surface channeling approximation (ASCA), where the slow motion perpendicular to the surface and the fast motion parallel to the axial channel are decoupled. Only the diffraction with reciprocal lattice vector exchange along the x axis, i.e., perpendicular to the atomic rows forming the axial channel is possible [22,25,31,38–43]. Thus, in contrast to HAS, the "effective" projectile-surface interaction potential appears averaged along the axial channel, and the complex 3D diffraction problem reduces to the 2D diffraction of slow projectiles with energy

$$E_{2D} = E - k_y^2/2M = \left(k_x^2 + k_z^2\right)/2M, \qquad (1)$$

where $k_y = k\cos\phi\cos\Gamma$ is the momentum component of the incident beam along the low-index direction, and $k_x = k\cos\phi\sin\Gamma$ is the momentum component of the incident beam along the x axis.

The diffraction pattern is observed only when the misalignment angle Γ is small [44–46]. When $\Gamma = 0$, the incident beam is perfectly aligned with the low-index crystal direction, and the diffraction spots lie along the gray Laue circle as shown in Fig. 3. If the alignment is not perfect the diffraction spots are located on a bigger Laue circle (black) with its center shifted due to the misalignment angle Γ. Note that the image on the detector corresponds to a projected velocity map of the scattered projectiles and therefore to a reciprocal space image. The scattering geometry is completely determined as soon as the incidence angle ϕ and azimuthal angle Γ are known and these two angles are readily measured in each diffraction image. The position of the primary beam can be measured before inserting the surface into the beam or, alternatively the surface may be inserted only partially, leaving a small fraction of the direct beam unaffected.

In Fig. 4, we show a typical diffraction image obtained with an incident 400 eV ^{4}He atom beam aligned close to the [1$\bar{1}$0] direction of the $\beta_2(2\times4)$ reconstructed GaAs(001) surface. Bright diffraction spots are located along the well-defined half Laue circle of radius $R = k\sqrt{\cos^2\phi\sin^2\Gamma + \sin^2\phi}$ centered at (x_c,z_c). The bright spot in the lower half of the image corresponds to the fraction of the direct beam that did not hit the surface. The vertical solid white line connects the specular spot to the direct beam. The azimuthal angle Γ is given by the distance between the center of the Laue circle and the vertical white line. The incidence polar angle ϕ is given by half of the length of the vertical white line. The data allow direct measurement of the lattice period in the x-direction $L_x = 16.1$ Å. This corresponds to the polar angle difference between two neighbor diffraction spots of 4.47×10^{-4} rad, and a momentum exchange $G_x = 2\pi/L_x = 0.392$ Å^{-1}. Here, G_x is the reciprocal lattice parameter in the x-direction perpendicular to the axial channel. Thus the misalignment

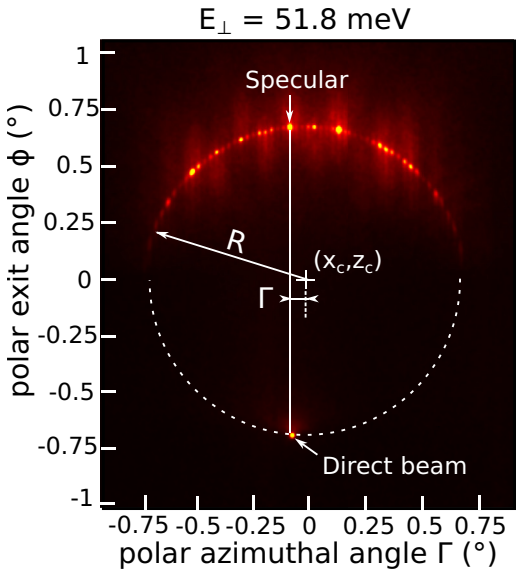

FIG. 4. (Color online) Diffraction image recorded for 400-eV helium atoms impinging at the $\beta_2(2\times4)$ reconstructed GaAs(001) surface. The incident beam is oriented with an incidence angle $\phi = 0.65^\circ$ ($E_\perp = 51.8$ meV), and with a misalignment angle $\Gamma = 0.06^\circ$ with respect to the $[1\bar{1}0]$ direction. The diffraction spots are located along the Laue circle of radius R, centered at (x_c,z_c). The vertical white line linking the specular and the direct beam spots is the intercept with the scattering plane.

angle Γ when expressed in momentum via $\sin\Gamma \approx \Gamma \approx (k_x/k)$ corresponds to the momentum component of the incident beam $k_x \approx -2G_x$. The misaligned incidence is at the origin of the asymmetry of the diffraction image with respect to the center of the Laue circle (x_c,z_c).

Figure 5 shows the integrated intensity taken along the Laue circle, as obtained from the diffraction image shown in Fig. 4 by applying a polarlike transform that converts the Laue circle into a line. The integration window is 2.5 mrad, equivalent to the measured FWHM of the direct beam. The relative intensities of each diffraction order are extracted

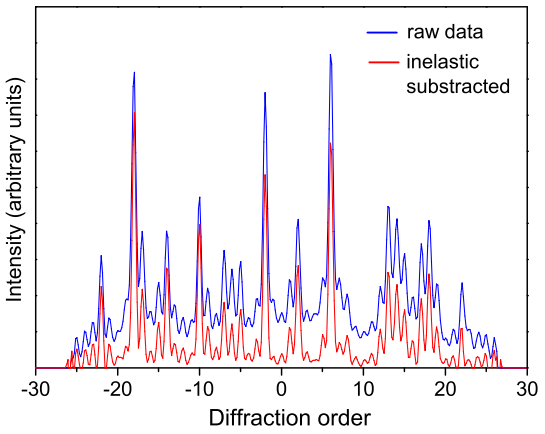

FIG. 5. (Color online) The raw intensity profile taken along the Laue circle from the diffraction image (Fig. 4) is given by the blue dashed line. The intensity after the inelastic contribution has been interpolated and substracted is given by the red solid line.

by fitting each peak to a Voigt profile. This Voigt profile is a simple convolution of a Lorentzian function with a Gaussian one, where the latter is the experimental resolution measured directly on the beam profile. Depending on the total and perpendicular energy, the intensity below and above the Laue circle can become quite significant compared to the intensity on the Laue circle itself. The analysis of this diffuse intensity, which also displays clear diffraction features with elongated streaks separated by G_x, is beyond the scope of the present paper. When needed this diffuse contribution to the intensity on the Laue circle can be subtracted (see Fig. 5) by interpolating its dependence on ϕ below and above the Laue circle. The error in the measurement of the relative intensity of the peaks is estimated to be only a few percent, mainly due to nonuniformity in the detector response. By carrying out measurements under conditions of uniform illumination using background sources such as ion gauges in the chamber, a correction to the detector response to recover a spatially uniform response has been applied. The images reported here correspond to regions of the detector where the correction made is less than 30% of the measured intensity.

B. Theoretical methods

1. Calculation of the diffraction intensities

In our theoretical approach, we consider the scattering of ^{4}He atoms from a perfect rigid $\beta_2(2\times4)$ reconstructed GaAs(001) surface, with a grazingly incident projectile beam aligned close to the $[1\bar{1}0]$ axial channel. The problem can be described in a single-particle picture by the stationary Schrödinger equation for the projectile wave function Ψ,

$$H\Psi(\mathbf{r}) = E\Psi(\mathbf{r}), \tag{2}$$

with total energy E and Hamiltonian

$$H = -\nabla^2/2M + V(\mathbf{r}), \tag{3}$$

where M is the projectile mass, and $V(\mathbf{r})$ is the projectile-surface interaction potential periodic in the (x,y) plane parallel to the GaAs(001) surface. We use $\mathbf{r} = (x,y,z)$ to define the position of the He projectile with the z axis perpendicular to the surface and pointing into the vacuum and with the y axis along the axial channel. The $V(\mathbf{r})$ potential is obtained on the basis of the *ab initio* DFT study detailed in the next section.

The experimental observation of a single Laue circle for the present system and scattering conditions justifies the use of the axial surface channeling approximation (ASCA) [22,25,31,38–43]. The 3D scattering problem can be thus greatly simplified by considering 2D scattering of He projectiles by the potential averaged along the $[1\bar{1}0]$ axial channel:

$$V_{2D}(x,z) = \frac{1}{L_y}\int_0^{L_y} V(\mathbf{r})dy, \tag{4}$$

where L_y is the period along the y-direction. With replacement $V(\mathbf{r}) \to V_{2D}(x,z)$ in Eqs. (2) and (3) the problem has translational invariance. The wave function of the projectile can be sought in the form

$$\Psi(\mathbf{r}) = e^{ik_y y}\psi(x,z), \tag{5}$$

where $\psi(x,z)$ is the solution of the stationary Schrödinger equation:

$$\left[\underbrace{-\frac{1}{2M}\left(\frac{\partial^2}{\partial x^2}+\frac{\partial^2}{\partial z^2}\right)+V_{2D}(x,z)}_{H_{2D}}-E_{2D}\right]\psi(x,z)=0. \quad (6)$$

The energy E_{2D} of the slow motion in the (x,z)-plane perpendicular to the surface is given by Eq. (1) Note that at grazing incidence conditions $E \sim k_y^2/2M$ so that $E_{2D} \ll E$. Thus the fast motion along the y axis is factorized out. The problem reduces to the diffraction of slow projectiles with an energy E_{2D} by the 2D potential V_{2D} periodic in x coordinate.

Owing to the periodicity, the wave function $\psi(x,z)$ can be represented as a Fourier series:

$$\psi(x,z)=\sum_{j=-N/2}^{N/2} f_j(z)\frac{1}{\sqrt{L_x}}\exp[i(k_x+jG_x)x], \quad (7)$$

where L_x is the period, $G_x = 2\pi/L_x$ is the reciprocal lattice parameter, and N defines the maximum number of reciprocal lattice vectors involved in the treatment of the scattering problem. In the present case, we use typically $N = 200$. Substitution of Eq. (7) into the Schrödinger equation Eq. (6) results in a system of coupled equations for z-dependent coefficients $f_j(z)$ [47], which can be cast in matrix form as

$$\left[-\frac{\partial^2}{\partial z^2}+2M\,\mathbb{W}(z)\right]\mathbb{F}(z)=0, \quad (8)$$

where $\mathbb{F}(z)$ is a column vector of $f_j(z)$ coefficients, and the coupling matrix $\mathbb{W}(z)$ is given by

$$W_{j'j}(z)=\left[\frac{(jG_x+k_x)^2}{2M}-E_{2D}\right]\delta_{j'j} + \frac{1}{L_x}\int_0^{L_x} V_{2D}(x,z)e^{i(j-j')G_x x}dx. \quad (9)$$

Far from the surface in vacuum $V_{2D} = 0$, so that the $\mathbb{W}(z)$ matrix is diagonal, and the $e^{ijG_x x}/\sqrt{L_x}$ basis functions define the asymptotic states. The scattering (equivalently diffraction) channel j is open (o) when $(jG_x + k_x)^2/2M < E_{2D}$, i.e., free particle propagation is possible along the z axis with energy

$$E_\perp^j \equiv \frac{(k_{zj})^2}{2M}=E_{2D}-\frac{(jG_x+k_x)^2}{2M}. \quad (10)$$

When $E_\perp^j < 0$, the corresponding scattering channel is closed (c). Note that while $E_\perp$ defined earlier in the paper stands for the perpendicular energy of the *incident* beam, $E_\perp^j$ stands for the perpendicular energy of the *outgoing* jth *diffracted* beam. Similarly k_z stands for the perpendicular to the surface momentum of the incident projectiles, while k_{zj} stands for the perpendicular to the surface momentum in the jth diffracted beam. Obviously, for small momentum exchange with the lattice, $k_{zj} \approx k_z$.

The scattering matrix $\mathbb{S}$ comprising the full information on the population transfer between ingoing $\chi_{in} = \frac{1}{\sqrt{2\pi L_x}}\exp[i(jG_x + k_x)x - ik_{zj}z]$ and outgoing $\chi_{out} = \frac{1}{\sqrt{2\pi L_x}}\exp[i(mG_x + k_x)x + ik_{zj}z]$ states is calculated following the procedure described in detail in Ref. [48]. In brief, with N linearly independent initial conditions $\mathbb{F}(z_{ini})$, the coupled equations (8) are solved using the Numerov-Fox-Goodwin method. We start the z propagation close to the surface in the classically forbidden region. The wave functions $\mathbb{F}(z)$ are then propagated up to the large positive $z = z_0$ far in the vacuum region. Matching the calculated numerical solutions to the proper asymptotic form, allows the scattering matrix extraction:

$$\mathbb{A}\mathbb{F}(z_0)=k^{-1/2}\left[\begin{pmatrix}\exp(-ikz_0)\\ \mathbf{0}\end{pmatrix} - \begin{pmatrix}\exp(ikz_0) & \mathbf{0}\\ \mathbf{0} & \exp(-kz_0)\end{pmatrix}\begin{pmatrix}\mathbb{S}_{oo}\\ \mathbb{S}_{co}\end{pmatrix}\right], \quad (11)$$

where $\mathbb{A}$ is a $N \times N$ matrix, $k^{-1/2}$ is the diagonal $N \times N$ matrix, where the diagonal elements are given by $1/\sqrt{|2ME_{2D}-(jG_x+k_x)^2|}$. The diagonal matrices $e^{\pm ikz}$ have the dimension $N_o \times N_o$, where N_o is the number of open channels. The matrix elements are given by $[e^{\pm ikz}]_{jj'} = e^{\pm ik_{zj}z}\delta_{jj'}$, where the wave vector describing the asymptotic z propagation in the channel j, k_{zj} is defined by Eq. (10). The diagonal e^{-kz} matrix has a dimension $N_c \times N_c$, where $N_c = N - N_o$ is the number of closed channels. The matrix elements are given by $[e^{-kz}]_{jj'} = e^{-\sqrt{|2ME_{2D}-(jG_x+k_x)^2|}z}\delta_{jj'}$.

The $N_o \times N_o$ matrix $\mathbb{S}_{oo}$ is the scattering matrix. The matrix elements $|(\mathbb{S}_{oo})_{jj'}|^2$ give the diffraction probabilities from the incident j' to the outgoing j channel. Thus, when the incidence beam is perfectly aligned with the axial channeling direction, the intensities of the diffracted beams $\mathcal{R}_j$ are given by $\mathcal{R}_j = |(\mathbb{S}_{oo})_{j0}|^2$. The general matrix element $|(\mathbb{S}_{oo})_{jm}|^2$ corresponds to the diffraction probabilities for the misaligned incidence, where the misalignment angle with respect to the low index direction is given by $\Gamma \approx (mG_x + k_x)/\sqrt{2ME}$. In a single calculation, one obtains results for several misaligned incidence cases. Note that, following this approach, the diffraction order labeled zero in all the figures, is not the specular one but the one aligned with the axial channeling direction (Fig. 3).

2. *He-GaAs interaction potential*

For the present study, the projectile-surface interaction potential $V(\mathbf{r})$ has to be adequate over a wide range of projectile energies $E_\perp$ perpendicular to the surface: from a few meV, as in HAS experiments, up to several hundred meV. Because of the large number of atoms involved in the surface unit cell, the full *ab initio* study of the He atom interaction with GaAs(001) $\beta_2(2 \times 4)$ reconstructed surface becomes computationally heavy if the interaction potential $V(\mathbf{r})$ is required on a dense mesh in spatial coordinates. We then choose the following strategy allowing the computational effort to be reduced, and an efficient and precise interpolation of the *ab initio* potential to be obtained at any desired (x,y,z) point.

Firstly, *ab initio* density functional theory calculations are used to obtain the z-dependent potential $V_{DFT}(x_n,y_n,z)$ for a set of (x_n,y_n) impact points within the surface unit

cell. Secondly, the DFT data have been fitted using binary interaction potentials V_{Ga}, and V_{As} of the He projectile with Ga and As atoms, respectively,

$$V(\mathbf{r}) = \sum_{\mathbf{R}_{\mathrm{Ga}}} V_{\mathrm{Ga}}(\mathbf{r} - \mathbf{R}_{\mathrm{Ga}}) + \sum_{\mathbf{R}_{\mathrm{As}}} V_{\mathrm{As}}(\mathbf{r} - \mathbf{R}_{\mathrm{As}}), \qquad (12)$$

where the sum runs over the positions of the surface atoms [49–51]. The binary interaction potentials are cast in the Ziegler, Biersack, and Littmark (ZBL) form [52],

$$V_S(\mathbf{r}) = \frac{1}{r} \sum_{j=1}^{J_S} a_j^S \exp\left(-b_j^S r\right), \qquad (13)$$

where J_S defines a number of screened exponentials used in the potential expansion, and $S = (\mathrm{Ga,As})$ stands for the atomic species at the surface. The parameters $(a_j^{\mathrm{Ga}}, b_j^{\mathrm{Ga}})$ and $(a_j^{\mathrm{As}}, b_j^{\mathrm{As}})$ are obtained from a least squares fit to $V_{\mathrm{DFT}}(x_n, y_n, z)$ with $V(\mathbf{r} = (x_n, y_n, z))$ given by Eqs. (12) and (13). Once the parameters of the binary potentials are fixed, from the fit to the *ab initio* calculations, Eq. (12) provides the interaction potential between the He projectile and the $\beta_2(2 \times 4)$ reconstructed GaAs(001) surface for any projectile position $\mathbf{r}$.

The *ab initio* He-surface interaction potential $V_{\mathrm{DFT}}(x_n, y_n, z)$ was computed through DFT within the generalized gradient approximation in the PW91 version [53] as implemented in the VASP code [54]. In the calculations we used the provided projector augmented-wave pseudopotentials [55] for Ga, As, and He, with a cutoff as high as 400 eV for the expansion of the Kohn-Sham orbitals. A $(1 \times 2 \times 1)$ Monkhorst-Pack grid centered at $(1/4, 1/4, 0)$ was used to sample the supercell, which yields four special points in the irreducible wedge of the 2D Brillouin zone corresponding to the $\beta_2(2 \times 4)$ reconstructed GaAs(001) surface. The GaAs slab was accurately constructed in order to fulfill the electron counting rule and avoid any problem that could stem from the polar character of the alternating stacking of Ga and As planes along the surface normal. The slab comprises the (1×1) surface unit cell and it is 13-layers thick, with a fixed central As layer; its upper surface showed the $\beta_2(2 \times 4)$ reconstruction while the bottom surface showed a rotated $\alpha(2 \times 4)$ reconstruction, both of which are As-rich. The void region in the supercell was 20-Å thick. The laterally averaged electrostatic potential was checked to be symmetric around the slab center and no dipole corrections were necessary. After optimization, the surface geometry turned out to be essentially equivalent to previous studies [56]. The He atom was then placed on the previously relaxed $\beta_2(2 \times 4)$ surface at varying (x_n, y_n) positions and several heights z in the range 0.5–5 Å, and the He-surface interaction potential $V_{\mathrm{DFT}}(x_n, y_n, z)$ was accordingly computed.

The quality of the model fit to the *ab initio* data can be assessed from Fig. 6 where we show the results obtained along several $\mathbf{r} = (x_n, y_n, z)$ projectile trajectories with impact points (x_n, y_n) indicated in Fig. 7. The parameters of the binary interaction potentials are given in the Table I. Note that in the potential construction procedure, we have used the repulsive part of the *ab initio* data as calculated with DFT, while the attractive part has been scaled: $V_{\mathrm{DFT}} \to 0.4 V_{\mathrm{DFT}}$, for $V_{\mathrm{DFT}} < 0$. This is because from the detailed comparison between the experimental and theoretical diffraction charts

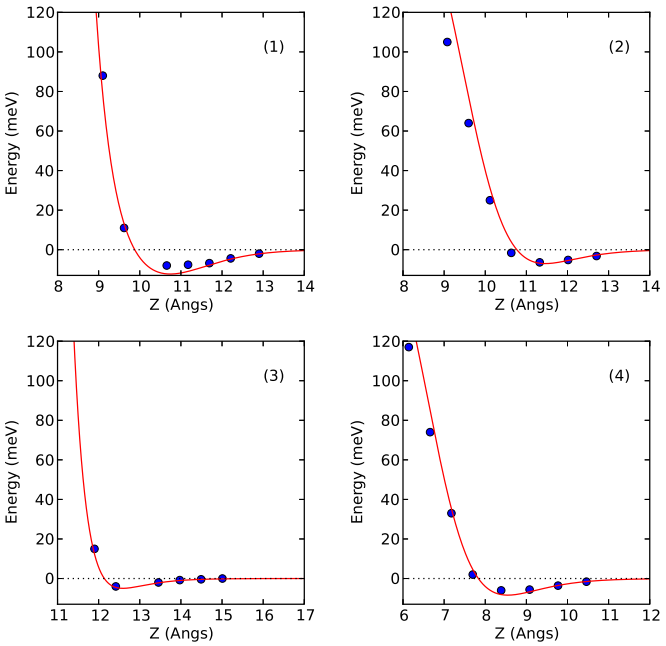

FIG. 6. (Color online) The *ab initio* results $V_{\mathrm{DFT}}(x_n, y_n, z)$ (dots) and the parametric fit given by Eqs. (12) and (13) (lines) for the interaction potential between He projectile and the $\beta_2(2 \times 4)$ reconstructed GaAs(001) surface. Results are shown as a function of the projectile surface distance z measured from the central As layer of the 13-layer-thick GaAs slab as used in the DFT calculations. Prior to the fit, the attractive part of the DFT data has been scaled as explained in the main text so that the theoretical diffraction charts match the experimental ones at low $E_\perp$ [see Sec. II B 2]. Different panels of the figure correspond to the different impact points (x_n, y_n) at the surface as indicated in Fig. 7.

(see Results and Discussion section), it appeared that the present DFT calculations overestimate the attractive part of the projectile-surface interaction. The above scaling of the DFT result yields a $V(\mathbf{r})$ potential that allows an excellent agreement between the calculated and measured diffraction charts to be reached. It is noteworthy that the resulting depth of the attractive potential well of -8.7 meV is in line with earlier reports [16,57]. We would like to stress here that the scaling of the attractive part of the *ab initio* potential has a significant effect only on the calculated diffraction patterns obtained with the perpendicular energies of the incident projectiles $E_\perp < 30$ meV. At higher perpendicular energies, the results are mainly determined by the repulsive part of the projectile-surface interaction. Using the scaled or raw DFT data as inputs to the quantum calculation leads then to very similar diffraction charts.

In Fig. 7(a), we show the final projectile surface interaction potential $V_{2\mathrm{D}}(x, z)$ used in the coupled channel calculation within the axial channeling approximation. Figure 7(b) shows the surface corrugation as seen by the 120-meV projectile, i.e., the equipotential surface map $\mathcal{Z}(x, y)$, where $\mathcal{Z}$ is taken such that the full 3D potential $V(x, y, \mathcal{Z}) = 120$ meV. For the $[1\bar{1}0]$ incidence direction, the most prominent structure is a deep axial channel located at the middle of the unit cell and formed by two atomic layer high steps. This strong corrugation of the $\beta_2(2 \times 4)$ reconstructed GaAs(001) surface together with

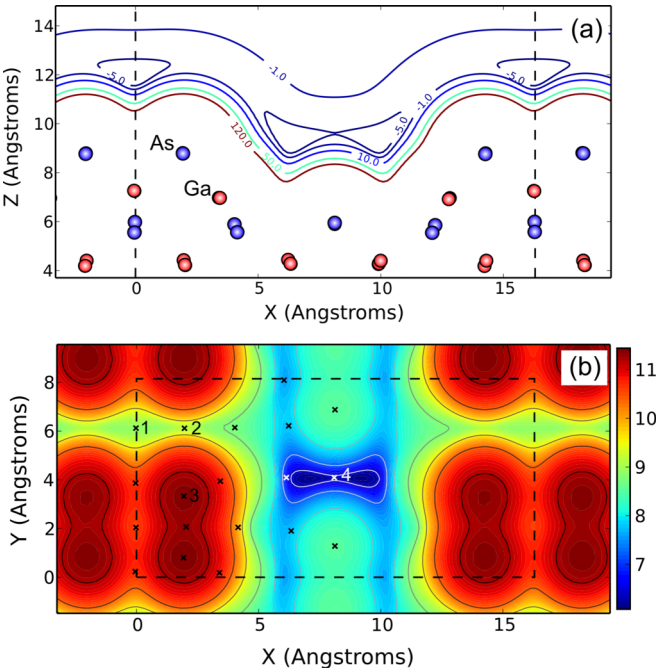

FIG. 7. (Color online) (a) The contour plot of the averaged projectile-surface interaction potential $V_{2D}(x,z)$. The label of the contour lines give the potential in meV. Vertical dashed lines separated by L_x delimit a unit cell. Atoms used in the *ab initio* studies are sketched with blue (As) and red (Ga) dots. (b) Surface corrugation function $\mathcal{Z}(x,y)$ as function of the x and y coordinates parallel to the $\beta_2(2\times4)$ reconstructed GaAs(001) surface. $\mathcal{Z}(x,y)$ is defined such that the full 3D potential $V(x,y,\mathcal{Z}) = 120$ meV. The surface unit cell is shown with dashed lines. Crosses indicate the impact points (x_n,y_n) used for the DFT calculation of the potential $V_{\rm DFT}(x_n,y_n,z)$. The numbered impact points correspond to the panels of Fig. 6.

a large period along the x direction perpendicular to the beam ($L_x \approx 16$ Å) is at the origin of the very rich diffraction pattern with a large number of populated diffraction orders as observed experimentally.

Indeed, within the axial channeling approximation, the semiclassical approach with sinusoidal hard wall model of the surface [21,22,58–60] leads to a simple expression for the intensity of different diffraction orders $\mathcal{R}_j$:

$$\mathcal{R}_j = J^2_{|j|}\left(\frac{k_z + k_{zj}}{2}\Delta_z\right), \tag{14}$$

where Δ_z is the amplitude of the surface corrugation $\mathcal{Z}(x,y)$ averaged along the low-index y-direction, and $J_{|j|}$ is the Bessel function of rank $|j|$, with $\pm j$ orders being degenerate. The wave vector k_{jz} is given by Eq. (10). Obviously, with increasing lattice period L_x and with increasing surface corrugation Δ_z, the number of efficiently populated diffraction orders increases, reaching up to 80 ($j = \pm 40$) under the present experimental conditions.

Along with the pronounced main channel at the middle of the unit cell, visible in Fig. 7(a), there is also a second shallow channel located at the unit cell boundary and running along the $[1\bar{1}0]$ direction between the two topmost As dimers. As we will discuss in the next section, the diffraction patterns result from the interference between the beams reflected from different substructures within the L_x unit cell. This is very similar to the physics reported in a recent FAD study of the oxygen covered Mo(112) surface [34]. In this respect, the presence of a second channel, even though comparatively shallow, leads to well defined features which allow a precise characterization of the surface geometry.

TABLE I. Parameters of the binary interaction potentials, given in Eq. (13), which have been used to fit the DFT data. $J_{\rm As} = 2$ and $J_{\rm Ga} = 1$. The amplitude a is given in atomic units of energy times a_0 and decay constant b is given in units of a_0^{-1}. a_0 stands for the Bohr radius.

$a_1^{\rm As} = 37.545$	$b_1^{\rm As} = 1.124$	$a_2^{\rm As} = -19.326$	$b_2^{\rm As} = 1.023$
$a_1^{\rm Ga} = 30.42$	$b_1^{\rm Ga} = 1.542$		

III. RESULTS AND DISCUSSION

Because of the strong surface corrugation and many open diffraction orders, the diffraction diagram appears extremely sensitive to both the incidence polar and misalignment angles. Figure 8 shows a drastic modification of the diffraction spectrum with many peaks switching from very intense to very weak and vice versa for only 0.03° difference in the incidence polar angle ϕ. The associated energy of the slow motion E_{2D} is only changed by few percent. Thus any significant variation of the effective surface corrugation as "seen" by the projectile is excluded. This extreme sensitivity can be easily understood as due to a simple wavelength variation on a comparatively long path difference between the beams reflected from the top and bottom of the potential valley: Δ_z, where $k_z\Delta_z \gg 1$. The change in incidence angle corresponds to a change in momentum k_z of 0.47 Å^{-1}, i.e., of only 4 %. However, a corrugation of $\Delta_z = 3.6$ Å [see Fig. 7(b)] is enough to induce a relative phase shift close to $\pi/2$. Similarly, at a fixed $E_\perp \sim 60$ meV a tiny variation of Δ_z of 0.13 Å leads to a phase shift close to $\pi/2$. For the GaAs $\beta_2(2\times4)$ surface, it follows from the calculated potentials that most of the evolution of the diffracted intensities with changing incidence

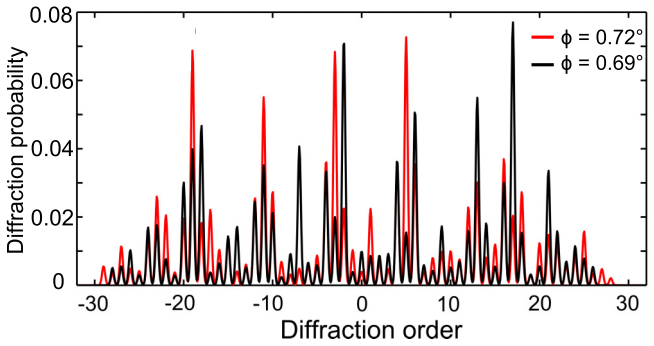

FIG. 8. (Color online) Deconvoluted diffracted intensities recorded for 400 eV He atoms at $\phi = 0.72°$, i.e., $E_\perp = 63$ meV (red line), and $\phi = 0.69°$, i.e., $E_\perp = 58$ meV (black line), incidence close to the $[1\bar{1}0]$ direction of the $\beta_2(2\times4)$ reconstruction of GaAs(001). The azimuthal misalignment angle $\Gamma = -0.06°$ corresponds to the transverse momentum k_x given by twice the primitive surface reciprocal lattice vector $k_x \approx -2G_x$.

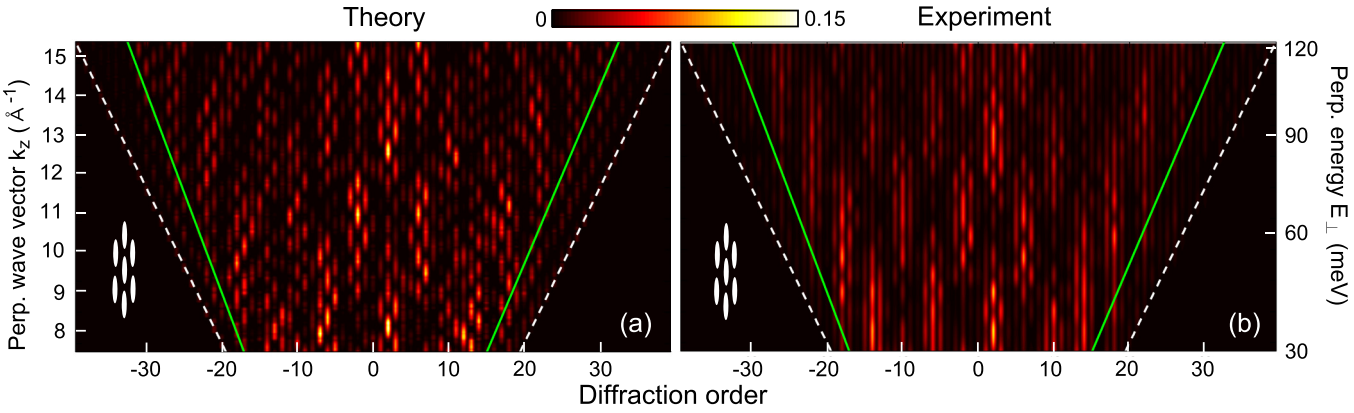

FIG. 9. (Color online) Diffraction charts for ^{4}He atoms incident along the $[1\bar{1}0]$ direction of the $\beta_2(2\times4)$ phase of GaAs(001). The azimuthal misalignment angle Γ is such that the momentum component of the incident beam $k_x \approx -2G_x$, where the reciprocal lattice parameter across the axial channel $G_x = 0.39$ Å^{-1}. The intensity of the diffracted beams is displayed as function of the diffraction order (horizontal axis) and perpendicular to the surface momentum of the incident beam k_z (vertical axis). The momentum k_z is measured in Å^{-1}. On the right vertical axis we give the corresponding perpendicular energy $E_\perp = k_z^2/2M$. The panels of the figure correspond to (a) theoretical $\mathbb{S}$-matrix calculations and (b) experimental data obtained by changing the incident angle at a constant total energy of 400 eV. The dashed lines delimit the region between closed and open diffraction channels. The green lines show the position of the classical rainbow due to the shallow potential valley between the two topmost As dimers.

angle can be understood in terms of probing an almost constant equipotential surface with a variable projectile wavelength.

A. Comparison of experimental and theoretical diffraction charts

The sensitivity to the details of the projectile-surface interaction and scattering geometry demonstrates the power of FAD as a surface analysis tool. However, this very high sensitivity complicates the comparison with theoretical calculations in the present system. Indeed, perfect match between the calculated and measured data for the fixed incidence conditions would require an extremely fine adjustment of the interaction potentials where the surface corrugation has to be determined with precision close to 0.01 Å (see discussion of Figs. 8 and 9 where a 0.1 Å variation of the corrugation amplitude is enough to switch the intensity of a diffraction peak from maximum to minimum). One way to handle this complexity is to bypass the fine details and to concentrate on the gross features of the evolution of the diffracted intensities with the wavelength $\lambda_z = 2\pi/k_z$ (or directly with wave vector k_z) characteristic for the slow motion perpendicular to the surface. Experimentally, this corresponds to a so-called rocking curve scan and in terms of interpretation to a diffraction chart [22] analysis. The diffraction charts allow a global analysis that is extremely helpful for qualitative and semiquantitative interpretation. Indeed, specific patterns can be identified and linked with main features of the surface reconstruction using a semiclassical approach. The most simple model is certainly ray tracing on a corrugated hard wall with corrugation $\mathcal{Z}(x)$ defined as the equipotential line: $V_{2D}(x,\mathcal{Z}(x)) = E_\perp$. Here, V_{2D} is the projectile-surface interaction within the axial surface channeling approximation introduced earlier. As we show below, such a ray tracing analysis provides a straightforward interpretation of the observed diffraction chart in the quasispecular region.

In Fig. 9, we show the experimental and theoretical diffraction charts for a ^{4}He atom beam incident along the $[1\bar{1}0]$ direction of the $\beta_2(2\times4)$ reconstructed GaAs(001) surface. The azimuthal misalignment angle Γ is such that the momentum component of the incident beam $k_x \approx -2G_x$. The perpendicular energy $E_\perp$ range covered by the data is 30–120 meV. The dashed lines $j_{\min}(k_z)$ and $j_{\max}(k_z)$ delimit the region between the closed and open diffraction channels, where for the latter the allowed diffraction orders j are within the range $j_{\min} \leqslant j \leqslant j_{\max}$, as can be obtained for fixed k_z, or equivalently $E_\perp$ from Eqs. (1) and (10).

A rich diffraction pattern is obtained with many populated diffraction orders j showing a fast variation of the diffraction intensity with k_z. Note that because of the small misalignment Γ, the diffraction charts are slightly asymmetric with respect to $j = 0$. As a main observation, the experimental and theoretical diffraction charts plotted at the same absolute scale are in excellent overall agreement as far as the main features are concerned. In particular, this is the case for the two link chain pattern forming the brightest motif of the data at small diffraction orders, and highlighted in white at the bottom left of the panels of the figure. This pattern appears every eight diffraction orders in k_x and every 4.5 Å^{-1} in k_z with two sets in quadrature, i.e., shifted by four diffraction orders in k_x and 4.5/2 Å^{-1} in k_z. We stress here that we used the geometry obtained in DFT calculations and no *a posteriori* adjustment of the atomic positions [31–33] has been attempted.

B. Semiclassical analysis of the quasispecular scattering

Despite the complexity of the diffraction charts, many of the observed features can be easily rationalized as due to specific structures in the projectile-surface interaction potential. We start with the semiclassical analysis of the quasi-specular region defined by a moderate exchange of transverse momentum k_x, and corresponding to the central part of the Laue circle. As stressed above, for the FAD diffraction conditions, the axial channeling approximation applies. The problem reduces to the diffraction of slow projectiles with

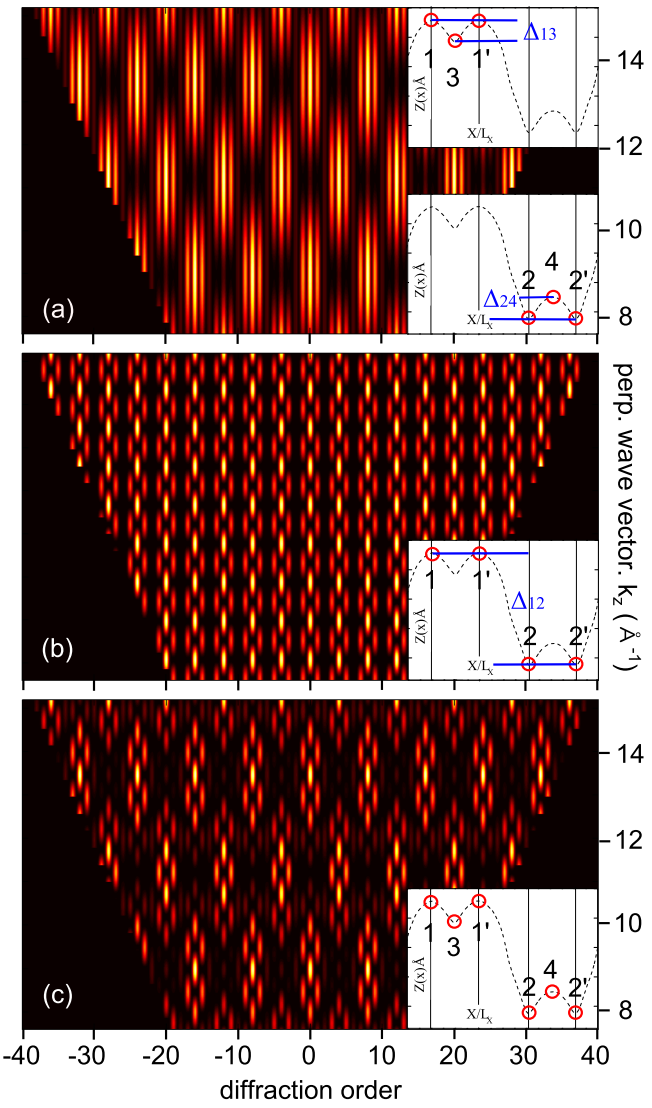

FIG. 10. (Color online) Sketch of the semiclassical analysis based on quasispecular reflection from the flat sections of the corrugation function $\mathcal{Z}(x)$ calculated for $E_\perp = 100$ meV. (a), (b), and (c) show the diffraction charts associated with the color points depicted in the respective insets where vertical bars are separated by $L_x/4$. In (a), the low-frequency modulation originating from the isolated secondary valleys is outlined. Taking $\Delta_{13} = \Delta_{24}$, the same diffraction chart is obtained either from the top valley [points (1), (2), and (1′)] or from the bottom one [points (2), (4), and (2′)]. The diffraction chart in (b) outlines the high frequency components resulting from the topmost and bottommost sections. In (c), all six flat sections are included reproducing the two-link chain pattern.

energy E_{2D} by the $V_{2D}(x,z)$ potential obtained by averaging $V(\mathbf{r})$ along the axial channel. In the following, we will neglect the small experimental misalignment of the incident beam with respect to the axial channel direction, and consider a hard wall potential model shown in Fig. 10. The incident projectiles with momentum k_z are diffracted by the hard wall located at $z = \mathcal{Z}(x)$, where $V_{2D}(x,\mathcal{Z}(x)) = k_z^2/2M$.

In terms of trajectories, the diffraction with small momentum exchange $jG_x = j2\pi/L_x$ (j small) along the x axis is dominated by the contribution of the "flat sections" at the maxima and minima of the corrugation function $\mathcal{Z}(x)$ such that $d\mathcal{Z}(x)/dx = 0$. These are marked with dots in Fig. 10. The phase difference between two rays reflected at locations x_m and x_n is

$$\alpha_m - \alpha_n = jG_x(x_m - x_n) + 2k_z(\mathcal{Z}(x_m) - \mathcal{Z}(x_n)), \qquad (15)$$

where for small j, we have neglected the change in the momentum k_z after reflection. Equation (15) takes into account that for a periodic structure only trajectories with a k_x momentum exchange given by the reciprocal lattice vector will contribute to the final result. Finally, the hard wall profile dependence on $E_\perp$ is neglected here. This is a reasonable approximation, supported by the calculated equipotential lines of the V_{2D} potential shown in Fig. 7(a), and fully sufficient for the present qualitative discussion. Considering a local scattering cross section $A = \left|d^2\mathcal{Z}(x)/dx^2\right|^{-1}$ (i.e., the local curvature), the scattering intensities can be calculated as

$$\mathcal{R}_j = \left|\sum_f \sqrt{A_f}\exp(i\alpha_f)\right|^2, \qquad (16)$$

where the sum runs over the "flat sections" of the surface. In what follows, to keep the discussion as simple as possible, we will assume $A_f = 1$.

Using Eqs. (15) and (16), we are now in a position to assign structures on the diffraction chart to trajectories bouncing on different parts of the corrugated surface. We start with analysis of the trajectories reflected at positions (1) and (1′), which are located at the same $\mathcal{Z}$, and delimit the shallow potential valley between the two topmost As dimers. Since $\mathcal{Z}(x_1) = \mathcal{Z}(x_{1'})$, the corresponding trajectories are always in phase for specular reflection ($j = 0$). The separation in x is $x_{1'} - x_1 = L_x/4$ so that the phase differences evolve with reciprocal lattice vector exchange as $\Delta\alpha = \alpha_{1'} - \alpha_1 = j\pi/2$. The diffraction orders $j = 4n + 2$, (n = integer), correspond to a phase difference of π and will thus be extinguished due to destructive interference at all k_z. The orders with $j = 4n$ will be the brightest.

Introducing now the trajectories emerging from (3), the bottom of the shallow potential valley between (1) and (1′), an oscillating structure appears along k_z in the diffraction chart. It is associated with the phase difference $2k_z\Delta_{13}$, where $\Delta_{13} = \mathcal{Z}(x_1) - \mathcal{Z}(x_3)$ [see Fig. 10(a)]. All together the patch motif of the diffraction chart is obtained with clear similarities with experimental data. Since $x_3 - x_1 = x_{1'} - x_3 = L_x/8$, the patch structure is repeated every eight diffraction orders. Note, however, that patches are also observed every four diffraction orders but in quadrature with respect to k_z because at these k_z values the π phase shift associated with four primitive reciprocal lattice vectors exchange in x direction is exactly compensated by a π phase shift due to the change in k_z.

When considering the scattering from the three points [(2), (2′), and (4)], one obtains exactly the same diffraction chart as for the [(1), (1′), and (3)] sequence. This is because the underlying atomic arrangements are similar, i.e., a Ga atomic row sandwiched between two protruding As atomic rows in the direction of the beam (see Fig. 7). Since, from the calculated DFT potential we see that $\Delta_{13} = \Delta_{24}$,

and since the separations in x between the points are also given by $L_x/8$: $x_4 - x_2 = x_{2'} - x_4 = L_x/8$, both the vertical and horizontal modulations are identical. We have explicitly checked that setting $\Delta_{13} \neq \Delta_{24}$ rapidly blurs the diffraction chart and degrades its comparison with experiment. Note that while the analysis is strictly speaking applicable only for the quasispecular region, we show the full diffraction chart for the sake of completeness.

As expected, the highest-frequency component $\Delta k_z \approx 0.9$ Å^{-1} observed for all diffraction orders in experimental and full-quantum theoretical diffraction charts emerges from the maximum separation in z between the scatterers. This is illustrated in Fig. 10(b) by considering only the trajectories bouncing on the topmost and bottommost points, i.e., (1), (1′) and (2), (2′). The phase difference associated with motion perpendicular to the surface is given by $2k_z\Delta_{12}$, where $\Delta_{12} = \mathcal{Z}(x_1) - \mathcal{Z}(x_2) = 3.6$ Å. This explains the fast oscillating structure. As to the chain pattern where adjacent diffraction orders are in quadrature, this emerges naturally from the $L_x/2$ separation in x between the pairs of points [(1), (1′)] and [(2), (2′)], and from the $L_x/4$ separation in x between between (1) and (1′), as well as (2) and (2′) points within each pair. For the fixed k_z, the phase difference between the pairs of scatterers is $\alpha_2 - \alpha_1 = \alpha_{2'} - \alpha_{1'} = j\pi$ so that each $j = 2n$ ($n =$ integer) diffraction order corresponds to constructive interference and should be intense. However, as discussed above, each $j = 4m + 2$ ($m =$ integer) order will be extinct because of the destructive interference between the rays reflected from the points within each pair. Two conditions lead to the conclusion that $j = 4n$ orders will be bright. Now, assuming $j = 4n$, changing $j \rightarrow j \pm 1$ leads to the π phase shift between [(1), (1′)] and [(2), (2′)] pairs, which can be compensated by k_z change by $\Delta k_z/2$. Note that the (1) and (1′), as well as (2) and (2′) points are dephased by $\pi/2$ so that the resulting spots are less bright than these at $j = 4n$.

The complete model where trajectories bouncing on the six points discussed above are considered is displayed in Fig. 10(c). It shows the two link chain pattern inside the patch structure, as actually observed experimentally and calculated using full quantum scattering matrix approach.

The simple model discussed above outlines physical parameters both for the surface morphology and for the diffraction structure. It means, for instance, that at 135 meV perpendicular energy, the wavelength $\lambda = 0.36$ Å is ten times smaller than the corrugation so that the surface can be seen as a grating with very deep groove. The model also indicates that both Δ_{13} and Δ_{24} corrugation parameters should be close to each other and close to $\Delta_{12}/5$ as can be derived from the ratio of the slow to fast vertical modulation in Fig. 9 (respectively, 0.9 and 4.5 Å^{-1}). This is fully supported by the *ab initio* potentials calculated in this work.

Let us summarize. For small reciprocal lattice vector exchange, the brightest pattern in the calculated and measured diffraction chart shown in Fig. 9 is the "two link chain pattern." For a fixed reciprocal lattice vector exchange (i.e., for a given diffraction order) the k_z dependence is characterized by the rapid oscillation with a period of ≈0.9 Å^{-1}. Globally, the $j = 4n + 2$ diffraction orders are extinct and the $j = 4n$ orders are most intense ($n =$ integer). This rapidly varying pattern is modulated by the slowly varying pattern with periodicity ≈4.5 Å^{-1} in k_z and $8G_x$ ($j = 8n$) in the transverse momentum exchange direction. The above result can be explained by a simple model where six scattering structures are located at coordinates (x_f, z_f) corresponding to the flat regions of the corrugation function and which are given by (1,1),(2,4/5),(3,1),(5,0),(6,1/5),(7,0) where x_f is in $L_x/8$ units with $L_x \approx 16$ Å the lattice parameter and z_f is scaled by $\Delta_{12} = 3.6$ Å.

C. Large reciprocal lattice vector exchange

The pronounced surface corrugation of the GaAs $\beta_2(2\times4)$ reconstruction with a deep channel in the $[1\bar{1}0]$ direction shown as (1)-(2)-(2′)-(1′) in Fig. 10(a) leads to a non-negligible intensity of the diffracted beams almost parallel to the surface. Indeed, from energy conservation, the highest (+) and lowest (−) possible diffraction order j is given by

$$[(j \pm 1)G_x + k_x]^2/2M > E_\perp + k_x^2/2M, \qquad (17)$$

[cf. Eq. (10)] when the perpendicular energy of the outgoing beam $E_\perp^j$ is close to zero. Careful inspection of the calculated and measured data shows that these diffracted beams marked with dashed white lines in Fig. 9 represent about 1 % of the total intensity. Most of the FAD experiments reported so far have been performed on surfaces with small corrugation, where the classical rainbow angle is well below $\pi/2$ and the diffracted beams moving parallel to the surface are extinct [22,61,62]. In the present case, considering the slope $d\mathcal{Z}(x)/dx$ of the corrugation function between (1) and (2) in Fig. 10(a) one obtains a rainbow angle exceeding $\pi/2$. Thus some of the projectiles experience guiding with multiple collisions with walls of the main channel. We leave the detailed assessment of the multiple collision regime and its signature in diffraction charts for a future publication.

D. Attractive part of the projectile-surface interaction

At collision energies $E_\perp$ of 100-meV FAD "probes" the geometric arrangement of the surface atoms allowing a relatively straightforward interpretation of the gross features of the diffraction charts. When $E_\perp$ is reduced into the meV range, the interpretation of the data requires more careful consideration. In this regime, the diffraction becomes sensitive to fine details of the projectile-surface interaction potential, including the attractive part due to polarization vdW forces [11,12,15–18]. The latter is the origin of the attractive physisorption potential well, usually in the 10-meV range for He atoms incident on various surfaces [16,17,63]. The correct description of the vdW interaction has always been a challenge for *ab initio* theoretical approaches [63–68] so that the availability of experimental references is highly important.

Experimentally, HAS provided a high resolution window into the attractive physisorption potential well, in particular through the measurement of the energies of bound state resonances (BSRs) [11,50,51,69–73]. The BSRs are observed when the reciprocal lattice vector exchange with the surface leads to the projectile being trapped in bound states (BSs) at the surface. The motion perpendicular to the surface is then confined with quantized energies below the vacuum level $E_\ell < 0, (\ell = 1,2,\dots)$. The bound states have a finite

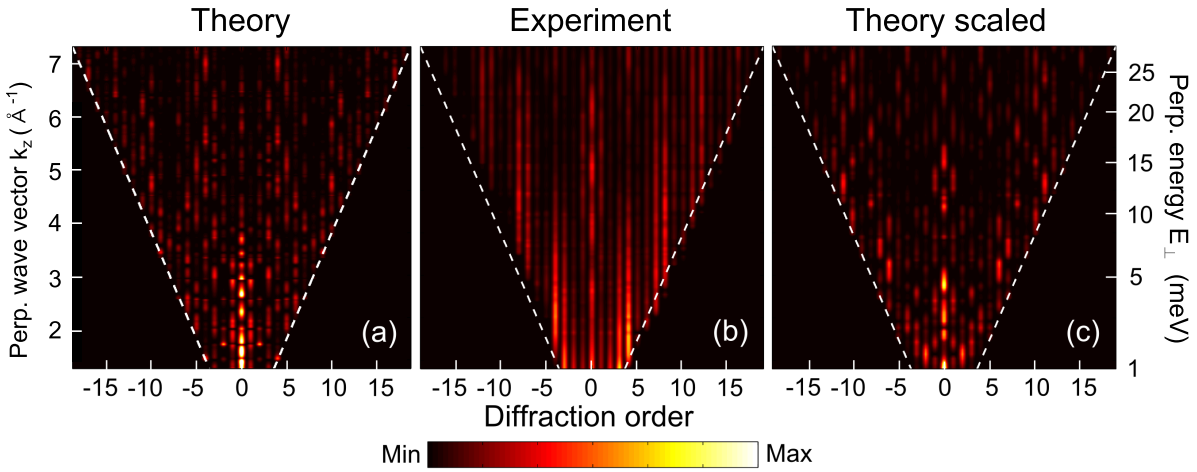

FIG. 11. (Color online) Diffraction charts at lower perpendicular energy compared to Fig. 9, for the same GaAs surface. The He perpendicular energy is now below 30 meV and the misalignment angle is here negligible ($\Gamma \sim 0$). The panels (a) and (c) of the figure display theoretical results and panel (b) displays the experimental data. The coupled channel calculations have been performed with atom-surface interaction potential: (a) directly obtained from the *ab initio* DFT study; (c) obtained by applying a 0.4 scaling factor to the attractive part of the DFT potential. The dashed lines delimit the region between closed and open diffraction channels.

lifetime, and a subsequent reciprocal lattice vector exchange with the surface allows the projectile to be released back into the vacuum. Based on empirical data for E_ℓ, one can either tune the parameters of the semiempirical density functional within the DFT scheme, or advanced model potentials can be developed which allow rather precise description of HAS experiments to be achieved over a broad range of scattering conditions [11,50,51]. Recently, we have demonstrated that the BSRs can be observed at low $E_\perp$ in FAD experiments on the LiF(001) surface allowing not only measurement of the energies of the BSs, but also discussion of decoherence processes at surfaces [75].

In the present case, we also found that FAD diffraction at very small incidence angles provides information on the attractive part of the projectile-surface interaction potential. In Fig. 11, we show the calculated and measured diffraction charts for ^{4}He atoms incident along the $[1\bar{1}0]$ direction of the $\beta_2(2\times 4)$ reconstruction of GaAs(001). We focus here on low collision energies $E_\perp < 30$ meV where the experimental data have been obtained by changing the incidence angle ϕ at a constant total beam energy of 400 eV. The full quantum coupled-channel calculations have been performed with the atom surface interaction potential $V_{2D}(x,z)$ obtained either directly from DFT calculations [panel (a)], or after applying a scaling factor of 0.4 to the attractive part of the DFT results [panel (c)]. For further details on the construction of the interaction potential we address the reader to the Sec. II B 2.

While we have explicitly tested that at large energies $E_\perp > 50$ meV, both scaled and nonscaled potentials give quite similar results, the low-energy part of the calculated diffraction charts displayed in Figs. 11(a) and 11(c) is qualitatively different. Using the original DFT inputs results in an irregular pattern with many BSRs as is particularly pronounced at low $E_\perp < 10$ meV. This reflects the relatively strong attractive part of the potential obtained in the present DFT calculations with a physisorption potential well approaching -18 meV. The "two link chain" structures discussed in the previous section are basically washed out. The above theoretical result is not supported by our experimental data shown in Fig. 11(b), where a continuous and smooth intensity variation can be seen with a clear "link chain" sequence visible at near specular scattering and low diffraction orders.

We find that in order to reproduce the experiment at low energies one has to correct the *ab initio* data by reducing the attractive part of the calculated atom-surface interaction. However, the repulsive part of the DFT projectile-surface interaction, corresponding to the surface corrugation "seen" by a projectile in the $E_\perp \geqslant 50$ meV range gives a good description of the measured diffraction charts and so should be preserved. The simplest way to comply with both requirements is to apply the scaling procedure $V_{DFT} \rightarrow 0.4 V_{DFT}$, for $V_{DFT} < 0$, where the smoothness of the final potential $V_{2D}(x,z)$ is guaranteed by the interpolation procedure given by Eqs. (12) and (13). The scaling allows the low-energy experimental data to be reproduced as is demonstrated by the calculated diffraction chart shown in Fig. 11(b). The role of the BSRs is strongly reduced and the "link chain" sequence is retrieved at low diffraction orders with the correct $E_\perp$ energy position of the intensity maxima. It is noteworthy that the resulting depth of the attractive potential well -8.7 meV, as obtained from the planar averaging of the potential is in line with earlier reports for the same system [16,57]. We also note in passing that the original and adjusted potential wells differ by only $\sim$12 meV, which is at the limit of the precision of DFT calculations. Our results thus suggest that the FAD experiments offer an interesting alternative to test *ab initio* approaches in atom-surface interaction studies. The advantage over HAS is that the FAD technique covers a larger $E_\perp$ energy range and that it can be used at high temperatures as demonstrated here.

IV. SUMMARY AND CONCLUSIONS

A GIFAD setup has been installed on the conventional RHEED ports of a molecular beam epitaxy chamber. This has

allowed the technologically useful $\beta_2(2\times4)$ reconstruction of the GaAs(001) surface at 530 °C under an As_4 overpressure to be measured in situ via the diffraction of ^{4}He projectiles incident close to the $[1\bar{1}0]$ direction. In addition, we have recently shown that this can allow real-time *in situ* monitoring of GaAs epitaxy [28]. The present study discusses high-resolution images of a strongly corrugated surface, where up to 80 diffraction orders have been observed. We show how the major characteristics of the surface reconstruction can be correlated to the gross features of the diffraction charts.

From the theoretical side, we have performed *ab initio* DFT studies of the interaction potential between He projectile and the $\beta_2(2\times4)$ phase of the GaAs(001) surface. These *ab initio* calculations have provided the input for a full quantum coupled-channel study of atom beam diffraction. In the FAD geometry, the fast motion parallel to the surface and the slow motion perpendicular to the surface are decoupled so that the axial channeling approximation can be used. The effective atom surface interaction potential appears averaged along the $[1\bar{1}0]$ axial channel. Only diffraction with reciprocal lattice vector exchange perpendicular to the atomic rows forming the axial channel is possible.

Direct comparison between the theory and experiment in this system is complicated because of "critical" behavior on both sides: the high sensitivity of the intensities of the numerous diffracted beams on the incidence geometry in experiment; and the high sensitivity of the calculated diffraction intensities to the details of the interaction potential. We then perform the global diffraction chart based analysis of the system. In the present case, it appeared extremely handy allowing to use the semiclassical model and to elucidate the main features of the surface relief that determine the diffraction.

We have chosen to present and discuss the measured and calculated diffraction charts in the form of two sets for high $E_\perp > 30$ meV and low $E_\perp < 30$ meV energies of the motion of incident projectiles perpendicular to the surface. At high energies where the results are very sensitive to the surface morphology, we have shown that the calculated and measured diffraction charts are in very good agreement taking into account the complexity of the system. This demonstrates the quality of the DFT-derived potentials in this energy range. The $\beta_2(2\times4)$ phase of the GaAs(001) surface appears to be an ideal playground allowing the observation of all the aspects of FAD reported so far: (i) rainbow, and supernumerary rainbows [22,74], (iii) several scattering structures within the unit cell [34], and (iv) bound state resonances [75]. Additionally, owing to the exceptionally high surface corrugation FAD reveals in this system new aspects of the projectile-surface interaction not reported so far in this scattering regime. These are (i) parallel to the surface exit of the diffracted beams and (ii) multiple rebounds at the channel walls (this latter issue is left for the future publication).

Comparison of the calculated and measured diffraction charts obtained at small $E_\perp$ energies below 30 meV highlights the overestimation of the attractive van der Waals potential well within the present DFT approach. The experimental data can be nicely reproduced via the rescaling of the attractive part of the DFT potential such that the resulting depth of the physisorption well is -8.7 meV, which is in line with earlier reports for the same system [16]. It is noteworthy that the higher $E_\perp$ energy part of the calculated diffraction charts is unaffected by the rescaling procedure. Our results thus suggest that FAD provides the possibility to quantitatively test *ab initio* models of atom-surface interactions in the van der Waals regime.

ACKNOWLEDGMENTS

We acknowledge funding from the Agence Nationale de la Recherche (Grants No. ANR-2011-EMMA-003-01 and No. ANR-07-BLAN-0160-01) as well as from the Triangle de la Physique (Grant No. 2012-040T-GIFAD). M. Debiossac and A. Zugarramurdi were in charge of the experimental and theoretical work, respectively, and contributed equally to this work.

[1] *Low-Energy Electron Diffraction*, edited by M. A. VanHove, W. H. Weinberg, and Ch-M. Chan, Springer Series in Surface Sciences Vol. 6, (Springer Verlag, Heidelberg, 1986).
[2] B. A. Joyce and D. D. Vvedensky, Mater. Sci. Eng., R **46**, 127 (2004).
[3] A. Ohtake, Surf. Sci. Rep. **63**, 295 (2008).
[4] V. P. LaBella, M. R. Krause, Z. Ding, and P. M. Thibado, Surf. Sci. Rep. **60**, 1 (2005).
[5] R. Feidenhans'l, Surf. Sci. Rep. **10**, 105 (1989).
[6] Y. Garreau, M. Sauvage-Simkin, N. Jedrecy, R. Pinchaux, and M. B. Veron, Phys. Rev. B **54**, 17638 (1996).
[7] I. Estermann and O. Stern, Z. Phys. **61**, 95 (1930).
[8] J. Toennies, Appl. Phys. A **3**, 91 (1974).
[9] T. Engel and K. H. Rieder, in *Structural Studies of Surfaces*, Springer Tracts Modern Physisc Vol. 91 (Springer-Verlag, Berlin, 1982), p. 55.
[10] E. Hulpke (ed.), *Helium Atom Scattering from Surfaces*, Springer Series in Surface Sciences Vol. 27 (Springer-Verlag, Berlin, 1992).
[11] H. Hoinkes, Rev. Mod. Phys. **52**, 933 (1980).
[12] D. Farías and K. H. Rieder, Rep. Prog. Phys. **61**, 1575 (1998).
[13] D. J. Riley, A. P. Jardine, S. Dworski, G. Alexandrowicz, P. Fouquet, J. Ellis, and W. Allison, J. Chem. Phys. **126**, 104702 (2007).
[14] M. J. Cardillo, G. E. Becker, S. J. Sibener, and D. R. Miller, Surf. Sci. **107**, 469 (1981).
[15] V. Bortolani and A. C. Levi, Riv. Nuovo Cimento **9**, 1 (1986).
[16] G. Vidali, G. Ihm, H.-Y. Kim, M. W. Cole, Surf. Sci. Rep. **12**, 135 (1991).
[17] R. D. Diehl, Th. Seyller, M. Caragiu, G. S. Leatherman, N. Ferralis, K. Pussi, P. Kaukasoina, and M. Lindroos, J. Phys.: Condens. Matter **16**, S2839 (2004).
[18] A. S. Sanz and S. Miret-Artés, Phys. Rep. **451**, 37 (2007).
[19] H. Khemliche, P. Roncin, and P. Rousseau, Patent No. WO2008003865A2 (2006).
[20] A. Schüller, S. Wethekam, and H. Winter, Phys. Rev. Lett. **98**, 016103 (2007).

[21] P. Rousseau, H. Khemliche, A. G. Borisov, and P. Roncin, Phys. Rev. Lett. **98**, 016104 (2007).
[22] H. Winter and A. Schüller, Prog. Surf. Sci. **86**, 169 (2011).
[23] P. Rousseau, H. Khemliche, N. Bundaleski, P. Soulisse, A. Momeni, and P. RoncinJ. Phys.: Conf. Ser. **133**, 012013 (2008)
[24] J. R. Manson, H. Khemliche, and P. Roncin, Phys. Rev. B **78**, 155408 (2008).
[25] F. Aigner, N. Simonović, B. Solleder, L. Wirtz, and J. Burgdörfer, Phys. Rev. Lett. **101**, 253201 (2008).
[26] A. C. Levi, J. Phys.: Condens. Matter **21**, 405004 (2009).
[27] H. Khemliche, P. Rousseau, P. Roncin, V. H. Etgens, and F. Finocchi, Appl. Phys. Lett. **95**, 151901 (2009).
[28] P. Atkinson, M. Eddrief, V. H. Etgens, H. Khemliche, M. Debiossac, A. Momeni, M. Mulier, B. Lalmi, and P. Roncin, Appl. Phys. Lett. **105**, 021602 (2014).
[29] N. Bundaleski, H. Khemliche, P. Soulisse, and P. Roncin, Phys. Rev. Lett. **101**, 177601 (2008).
[30] A. Schüller, M. Busch, S. Wethekam, and H. Winter, Phys. Rev. Lett. **102**, 017602 (2009).
[31] A. Schüller, S. Wethekam, D. Blauth, H. Winter, F. Aigner, N. Simonović, B. Solleder, J. Burgdörfer, and L. Wirtz, Phys. Rev. A **82**, 062902 (2010).
[32] J. Seifert, A. Schüller, H. Winter, R. Włodarczyk, J. Sauer, and M. Sierka, Phys. Rev. B **82**, 035436 (2010).
[33] A. Schüller, D. Blauth, J. Seifert, M. Busch, H. Winter, K. Gärtner, R. Włodarczyk, J. Sauer, and M. Sierka, Surf. Sci. **606**, 161 (2012).
[34] J. Seifert and H. Winter, Phys. Rev. Lett. **108**, 065503 (2012).
[35] B. Lalmi, H. Khemliche, A. Momeni, P. Soulisse, and P. Roncin, J. Phys.: Condens. Matter **24**, 442002 (2012).
[36] J. Seifert and H. Winter, Surf. Sci. **610**, L1 (2013).
[37] J. Seifert, M. Busch, E. Meyer, and H. Winter, Phys. Rev. Lett. **111**, 137601 (2013).
[38] M. S. Gravielle and J. E. Miraglia, Phys. Rev. A **78**, 022901 (2008).
[39] M. S. Gravielle, A. Schüller, H. Winter, and J. E. Miraglia, Nucl. Instr. Methods Phys. Res. B **269**, 1208 (2011).
[40] D. Farías, C. Díaz, P. Nieto, A. Salin, and F. Martín, Chem. Phys. Lett. **390**, 250 (2004).
[41] D. Farías, C. Díaz, P. Rivière, H. F. Busnengo, P. Nieto, M. F. Somers, G. J. Kroes, A. Salin, and F. Martín, Phys. Rev. Lett. **93**, 246104 (2004).
[42] A. Zugarramurdi and A. G. Borisov, Phys. Rev. A **86**, 062903 (2012).
[43] A. Zugarramurdi and A. G. Borisov, Phys. Rev. A **87**, 062902 (2013).
[44] A. Schüller and H. Winter, Nucl. Instrum. Methods Phys. Res. B **267**, 628 (2009).
[45] A. Ruiz, J. P. Palao, and E. J. Heller, Phys. Rev. A **79**, 052901 (2009).
[46] J. Seifert, A. Schüller, H. Winter, and K. Gärtner, Nuc. Instr. Methods Phys. Res. B **269**, 1212 (2011).
[47] J. R. Manson, *Theoretical Aspects of Atom-Surface Scattering*, edited by E. Hulpke, Springer Series in Surface Sciences Vol. 27 (Springer-Verlag, Berlin, 1992).
[48] D. W. Norcross and M. J. Seaton, J. Phys. B: At. Mol. Phys. **6**, 614 (1973).
[49] H. Winter, Phys. Rep. **367**, 387 (2002).
[50] V. Celli, D. Eichenauer, A. Kaufhold, and J. P. Toennies, J. Chem. Phys. **83**, 2504 (1985).
[51] P. W. Fowler and J. M. Hutson, Phys. Rev. B **33**, 3724 (1986).
[52] J. F. Ziegler, J. P. Biersack, and U. Littmark, *The Stopping and Range of Ions in Solids*, Vol. 1 (Pergamon, New York, 1985).
[53] J. P. Perdew, J. A. Chevary, S. H. Vosko, K. A. Jackson, M. R. Pederson, D. J. Singh, and C. Fiolhais, Phys. Rev. B **46**, 6671 (1992); **48**, 4978 (1993).
[54] G. Kresse and J. Hafner, Phys. Rev. B **47**, R558 (1993); **49**, 14251 (1994); **54**, 11169 (1996).
[55] G. Kresse and D. Joubert, Phys. Rev. B **59**, 1758 (1999).
[56] W. G. Schmidt and F. Bechstedt, Phys. Rev. B **54**, 16742 (1996).
[57] R. B. Laughlin, Phys. Rev. B **25**, 2222 (1982).
[58] U. Garibaldi, A. C. Levi, R. Spadacini, and G. E. Tommei, Surf. Sci. **48**, 649 (1975).
[59] R. I. Masel, R. P. Merrill, and W. H. Miller, Phys. Rev. B **12**, 5545 (1975).
[60] R. I. Masel, R. P. Merill, and W. H. Miller, J. Chem. Phys. **65**, 2690 (1976).
[61] J. D. McClure, J. Chem. Phys. **52**, 2712 (1970).
[62] S. Miret-Artésa and E. Pollak, Surf. Sci. Rep. **67**, 161 (2012).
[63] D.-L. Chen, W. A. Al-Saidi, and J. K. Johnson, J. Phys.: Condens. Matter **24**, 424211 (2012).
[64] L. W. Bruch, R. D. Diehl, and J. A. Venables, Rev. Mod. Phys. **79**, 1381 (2007).
[65] J. Tao and J. P. Perdew, J. Chem. Phys. **122**, 114102 (2005).
[66] J. Tao and A. M. Rappe, Phys. Rev. Lett. **112**, 106101 (2014).
[67] P. Hao, J. Sun, B. Xiao, A. Ruzsinszky, G. I. Csonka, J. Tao, S. Glindmeyer, and J. P. Perdew, J. Chem. Theory Comput. **9**, 355 (2013).
[68] S. Grimme, J. Antony, S. Ehrlich, and H. Krieg, J. Chem. Phys. **132**, 154104 (2010).
[69] H. Chow and E. D. Thompson, Surf. Sci. **59**, 225 (1976).
[70] P. Cantini and R. Tatarek, Phys. Rev. B **23**, 3030 (1981).
[71] J. G. Mantovani, J. R. Manson, and G. Armand, Surf. Sci. **143**, 536 (1984).
[72] J. A. Meyers and D. Frankl, Surf. Sci. **51**, 61 (1975).
[73] G. Derry, D. Wesner, S. Krishnaswamy, and D. Frankl, Surf. Sci. **74**, 245 (1978).
[74] A. Schüller and H. Winter, Phys. Rev. Lett. **100**, 097602 (2008).
[75] M. Debiossac, A. Zugarramurdi, P. Lunca-Popa, A. Momeni, H. Khemliche, A. G. Borisov, and P. Roncin, Phys. Rev. Lett. **112**, 023203 (2014).